Disorder effects on triple-point fermions

Hsiu-Chuan Hsu [1,2,*] Ion Cosma Fulga,[3] and Jhih-Shih You [4,†]

[1]*Graduate Institute of Applied Physics, National Chengchi University, Taipei 11605, Taiwan*
[2]*Department of Computer Science, National Chengchi University, Taipei 11605, Taiwan*
[3]*Institute for Theoretical Solid State Physics, IFW Dresden and Würzburg-Dresden Cluster of Excellence ct.qmat,*
Helmholtzstrasse 20, 01069 Dresden, Germany
[4]*Department of Physics, National Taiwan Normal University, Taipei 11677, Taiwan*

The stability of three-dimensional relativistic semimetals to disorder has recently attracted great attention, but the effect of disorder remains elusive for multifold fermions, that are not present in the framework of quantum field theory. In this paper, we investigate one type of multifold fermions, so-called triple-point fermions (TPFs), which have pseudospin-1 degrees of freedom and topological charges ± 2. Specifically, we consider the effect of disorder on a minimal, three-band tight-binding model, which realizes the minimal number of two TPFs. The numerically obtained, disorder-averaged density of states suggests that, within a finite energy window, the TPFs are robust up to a critical strength of disorder. In the strong disorder regime, the inter-TPF scattering is the main mechanism for destroying a single TPF. Moreover, we study the effects of disorder on the distribution of Fermi arcs and surface Berry curvature. We demonstrate that the Fermi arc retains its sharpness at weak disorder, but gradually dissolves into the metallic bulk for stronger disorder. In the clean limit, the surface Berry curvature exhibits a bipolar configuration in the surface Brillouin zone. With increasing disorder, the positive and negative surface Berry curvatures start to merge at the nearby momenta where the Fermi arcs penetrate into bulk.

I. INTRODUCTION

Fundamental particles in high-energy physics can emerge in condensed-matter systems. For example, Majorana fermions could be realized in topological superconductors [1], Dirac fermions in graphene [2] and Weyl fermions in topological semimetals [3]. These aforementioned quasiparticles are described by two-component spinors. Nonetheless, it has been shown that with particular crystal symmetries, lattice systems could host new types of quasiparticles with higher pseudospins [4,5], which have no high-energy counterparts. One of these exotic quasiparticles is realized as a low-energy excitation at a point where three energy bands become degenerate. The resulting threefold fermion has pseudospin-1 degrees of freedom, and has been dubbed the triple point fermion (TPF) [4]. TPFs have topological charges of ± 2, the same as that of double Weyl nodes. However, a TPF has three energy bands, two of which disperse linearly along any momentum direction, and one of which has a vanishing velocity at the band crossing point, i.e., it is a (locally) flat band. In crystals, a stable topological charge is separated from its partners with opposite charge in the Brillouin zone since the total charge must vanish as dictated by the Nielsen-Ninomiya theorem [6,7]. When two nodes of opposite topological charge are mixed, for instance, by

internode scattering, their topologically nontrivial properties are no longer guaranteed and can even disappear altogether.

The past few years have witnessed an enormous interest to understand the stability of the Weyl nodes against disorder [8–19]. The disorder-averaged density of states (DOS) has been used as an order parameter to characterize the stability of Weyl nodes. Within self-consistent Born approximation, it has been shown that there exists a critical disorder strength that separates the Weyl semimetal and diffusive metal regimes [14,15]. Meanwhile, numerical simulations performed using the kernel polynomial method revealed that the Weyl node is unstable, and the DOS becomes finite in the presence of disorder due to the rare region effects [13,16,20]. The stability of quadratic Weyl semimetals has also been investigated. It has been shown that linear Weyl semimetals are stable against random disorder, but the quadratic ones are not [12]. Similarly, Sbierski *et al.* [14] found that double Weyl nodes are unstable against correlated disorder. Although a TPF shares the same topological charge with the double Weyl point ± 2, the disorder effects in TPFs are still overlooked. It is an open question whether richer and more interesting physics will emerge in the TPFs when disorder and the additional flat band come into play.

A direct consequence of the topological charges is the existence of Fermi arcs connecting the surface projections of oppositely charged nodes. These Fermi arcs are manifestations of the bulk-boundary correspondence of Weyl semimetals and can be measured by angle-resolved photoemission spectroscopy [3] or in transport experiments [21]. Moreover, the Fermi arcs carry surface Berry curvature (BC)

*hcjhsu@nccu.edu.tw
†jhihshihyou@ntnu.edu.tw

245118-1

and Berry curvature dipole, leading to linear or nonlinear anomalous Hall conductivity [22,23]. So far, there are only few works devoted to studying the robustness of the Fermi arcs of Weyl semimetals [24–26]. Even less is known about the disorder effects on the Fermi arcs of TPFs.

Due to the additional flat band, the DOS, a commonly used diagnostic that indicates the stability of Dirac/Weyl nodes against disorder, cannot solely reveal the disorder effects on TPFs. Therefore, in addition to the DOS, we study the fate of Fermi arcs as well as the associated BC-driven phenomena. This paper is organized as follows. In Sec. II, we introduce the model Hamiltonian of the triple point fermion. The numerical results are presented and discussed in the following sections: Section III shows the results of density of states, and Sec. IV discusses the stability of Fermi arcs and the interplay between disorder and the surface Berry curvature. Finally, we conclude in Sec. V.

II. MODEL HAMILTONIAN

In this paper, we use the minimal lattice model that contains only a pair of triple point fermions [27]. This Hamiltonian, which is constructed as a combination between a double Weyl semimetal and a flat band at zero energy, reads

$$H_t(\vec{k}) = \begin{pmatrix} H_q & & \lambda_+^\dagger \\ & & \lambda_-^\dagger \\ \lambda_+ & \lambda_- & 0 \end{pmatrix}, \qquad (1)$$

where H_q is the three-dimensional (3D) momentum-space Hamiltonian for the double Weyl semimetal,

$$H_q(\vec{k}) = [2 - \cos(k_x) - \cos(k_y) - 2\cos(k_z)]\sigma_z$$
$$+ 2\sin(k_x)\sin(k_y)\sigma_y + 2[\cos(k_x) - \cos(k_y)]\sigma_x, \qquad (2)$$

σ_j are Pauli matrices, $\vec{k} = (k_x, k_y, k_z)$ is the momentum vector, and $\lambda_\pm = \lambda e^{i(\phi \pm \pi/4)}[\sin(k_x) \mp i\sin(k_y)]$ are the coupling terms between the double Weyl semimetal and the flat band. Hereafter, we set $\hbar = 1$ and the hopping energy and lattice constant to 1 for simplicity.

For the double Weyl semimetal H_q, the two bands near the Weyl nodes $(0, 0, \pm\pi/2)$ disperse linearly along k_z but quadratically along k_x and k_y. By introducing a flat band that couples to the double Weyl fermions, we obtain a triple point fermion [27] such that two of the bands disperse linearly in all momentum directions. The dispersion for $\lambda = 0.5$ along k_z at $(k_x, k_y) = (0, 0)$ is shown in Fig. 1(a). By Fourier transforming to real space, we obtain a tight-binding Hamiltonian which allows us to explore the effects of disorder.

The band crossings of H_t and H_q have the same topological charge [28], and the TPFs are protected by the combination of an anticommuting mirror symmetry about the $k_x = k_y$ plane and a C_4 rotation symmetry along the $k_x = k_y = 0$ axis [27]. This is the minimal model for TPFs with a symmorphic group [27]. Moreover, H_t and H_q are time-reversal symmetry broken and can be viewed as a stack of quantum anomalous Hall insulators along the k_z direction. The Chern number
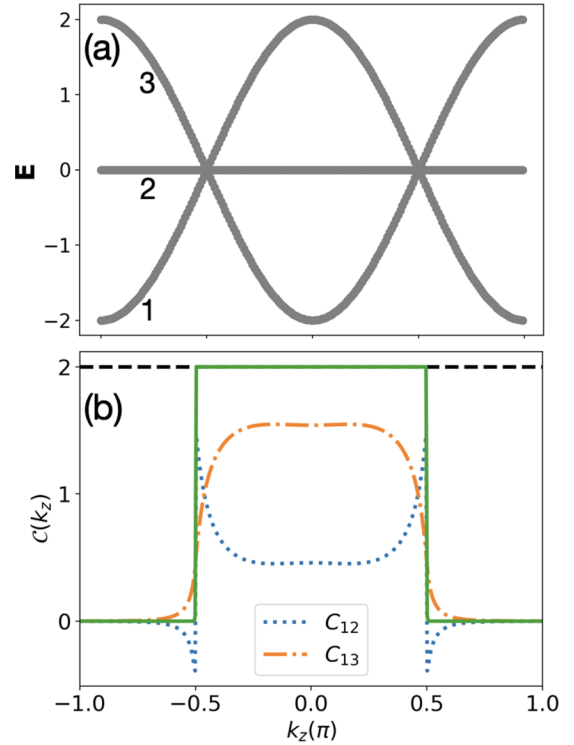

FIG. 1. (a) The energy dispersion for $\lambda = 0.5$ along k_z at $(k_x, k_y) = (0, 0)$. (b) The Chern number (green solid line) along k_z. The blue dotted (orange dashed dotted) line labeled by "12(3)" denotes the contribution to the Chern number obtained from the matrix element between the valence and the flat (conduction) bands. The dashed black line is a guide to the eye that shows the quantization of the total Chern number.

along k_z for the nth band is given by

$$\mathcal{C}^n(k_z) = \frac{1}{\pi} \int dk_x dk_y \Omega_z^n(\vec{k}), \qquad (3)$$

where $\Omega_z^n(\vec{k})$ is the z component of the Berry curvature for the nth band,

$$\Omega_z^n(\vec{k}) = -\mathrm{Im} \sum_{n \neq m} \frac{\langle n|v_x|m\rangle \langle m|v_y|n\rangle}{(E_n - E_m)^2}, \qquad (4)$$

where E_n and $|n\rangle$ are eigenenergies and Bloch eigenstates of the Hamiltonian $H_t(\vec{k})$, respectively, and $v_i = \partial H_t(\vec{k})/\partial k_i$ is the velocity operator. For H_t, the flat band does not carry a Chern number, whereas the lowest- and highest-energy bands carry opposite Chern numbers. For the lowest-energy band (band 1), there are two contributions to the Chern number. One is from the velocity matrix elements between bands 1 and 3, denoted by C_{13} and the other is between bands 1 and 2, denoted by C_{12}. The Chern number, Eq. (1), of the lowest-energy band at each k_z plane is shown by the green solid line in Fig. 1(b). It is well quantized between the two nodes. Both matrix elements 12 and 13 are nonzero for $\lambda = 0.5$. In contrast, when $\lambda = 0$, the topological charge is carried only by the double Weyl node, which is now decoupled from the flat band, and only the C_{13} component is nonzero. Therefore, as the coupling strength λ increases, there is a Berry curvature transfer between the bands as shown in Appendix A.

III. DENSITY OF STATES

A 3D relativistic semimetal has the low-energy dispersion $E = \pm v_f k$, where v_f is the slope of the band and $k = \sqrt{k_x^2 + k_y^2 + k_z^2}$. In the clean limit, it is straightforward to show that the DOS is $\rho_{\text{clean}}(E) = \frac{\pi^2}{2} k^2 (\frac{dk}{dE})^{-1} = \frac{\pi^2}{2v_f^3} E^2$. In the presence of disorder, the disorder-averaged DOS $\rho(E)$ at zero energy can serve as an order parameter for the disorder-driven semimetal-metal transition. For TPFs, bands 1 and 3 disperse linearly and, thus, the DOS of both bands still scales quadratically with energy [29]. However, due to the existence of the flat band, the DOS has an additional zero-energy peak. This is in stark contrast to the DOS of Weyl and Dirac fermions, and distinct phenomena arise from the TPFs with disorder.

To calculate the disorder-averaged DOS, we employ the kernel polynomial method [30] in the PYBINDING [31] package. Two types of disorder are considered. The first type is the white noise, which takes into account the scattering between the two TPFs. We add a random on-site potential $V(\vec{r})I_{3\times3}$ with $I_{3\times3}$ the 3×3 identity matrix, and $V(\vec{r}) \in [\frac{-W}{2}, \frac{W}{2}]$ drawn independently for each lattice site (indexed by real-space position vectors $\vec{r}$) from a uniform distribution, where W is the strength of disorder.

The second type is the correlated disorder,

$$H_c = \sum_i \sum_j \frac{W_j}{(\sqrt{2\pi}\xi)^3} e^{-(r_i - R_j)^2/2\xi^2} I_{3\times3} |i\rangle\langle i|, \quad (5)$$

where ξ is the correlation length, W_j is the random number given by a uniform distribution in the range $\in [\frac{-W}{2}, \frac{W}{2}]$, r_i is the position vector for a lattice site, and R_j is the position vector of an impurity. It is assumed that the number of impurity is the same as that of the lattice sites. When $\xi \to 0$, the correlated disorder reduces to the white-noise potential. As the correlation length ξ becomes larger, the scattering between two TPFs becomes weaker [14].

Figure 2(a) shows the results for white-noise disorder, computed for a cubic system consisting of L^3 sites with $L = 50$ and periodic boundary conditions imposed along all three directions. The zero-energy peak decreases and broadens as the disorder strength increases. As can be seen, there exists an energy range for which the DOS remains quadratic up to $W \leqslant 3$. In contrast, the double Weyl nodes have a linear DOS at finite energy in the presence of disorder [11,12,14]. Figure 2(b) shows the results for correlated disorder, using the same geometry. In contrast to white-noise disorder, the DOS is almost invariant to the disorder strength. This result suggests that the inter-TPF scattering is the main mechanism for destroying the single TPF physics.

We note that the TPF and multifold fermions have been predicted in a family of transition-metal silicides in which the multifold fermions are separated in energy [32]. Effectively, there is only one multifold fermion involved in scattering events. Thus, our results suggest that such a multifold fermion in this material family should be particularly robust against disorder.
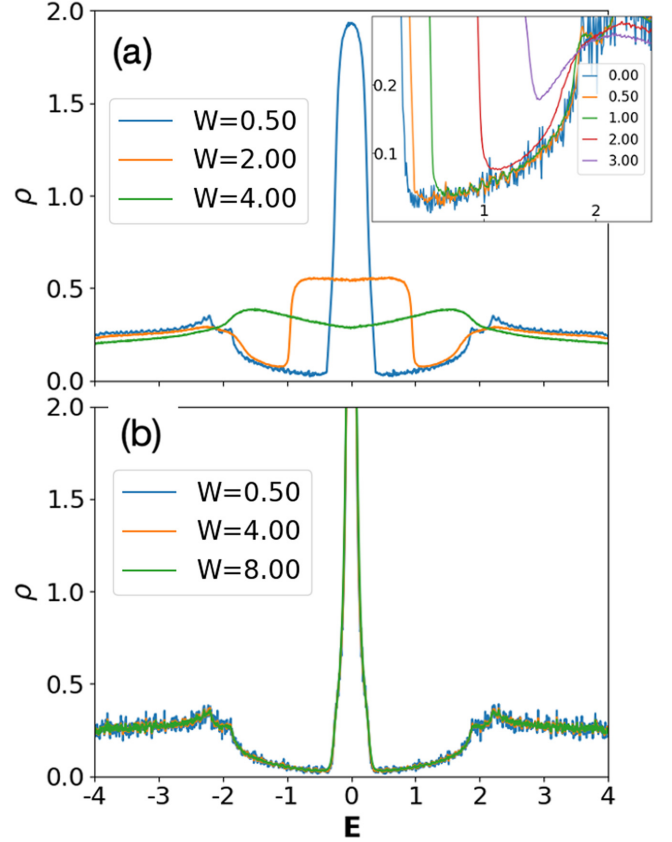

FIG. 2. The DOS as a function of energy for $\lambda = 0.5$ for a cubic system with a linear size of $L = 50$ lattice sites. A Gaussian broadening of 0.001 was used when implementing the kernel polynomial method, and the DOS was averaged over 20 disorder realizations. (a) DOS for the white-noise disorder. The inset is the zoomed-in plot showing the quadratic behavior of the DOS. (b) DOS for the correlated disorder with $\xi = 5$.

IV. FERMI ARCS

The existence of Fermi arcs is a consequence of the topological charges associated with the band crossing points. Several measurable quantities are related to the Fermi arcs and, thus, the stability of the Fermi arcs against disorder is an essential question. To study the topological surface states associated with the TPFs, we impose open boundary conditions along the x direction of the model Hamiltonian, whereas keeping the system infinite along the other two directions such that $k_{y,z}$ remain good quantum numbers. Since the central band is close to $E = 0$ and hinders the observation of Fermi arcs, here we focus on the Fermi arc state in a finite-energy range away from zero. The density of the Fermi arc states (ρ_a) in the clean limit is shown in Fig. 3(a). Here ρ_a is defined as

$$\rho_a(x, k_y, k_z) = \sum_{E_i \in [0.3, 0.3+\Delta E)} \sum_{o=1}^{3} |\langle \psi_i(k_y, k_z)|x, o\rangle|^2, \quad (6)$$

where $\psi_i(k_y, k_z)$ is the ith eigenvector with energy $E_i \in [0.3, 0.3 + \Delta E)$ at (k_y, k_z), x denotes the coordinate of lattice sites along the finite direction of the slab, and o labels the pseudospin degrees of freedom. Here ΔE was set to be 0.1 to ensure the continuity of the Fermi arcs in the projected
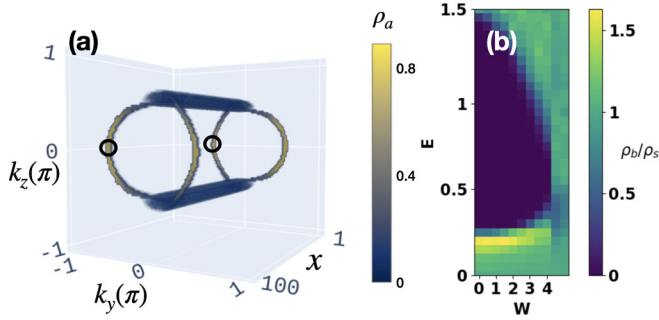
FIG. 3. (a) Distribution of states in the energy range of $0.3 \leqslant E < 0.4$ for $\lambda = 0.5$ in the absence of disorder. The black circles denote two of the furthest momenta away from the TPFs. (b) The ratios of the bulk and surface density near k' in a slab geometry. The number of lattice sites of the slab is 100 along the x direction, and we have averaged over ten disorder realizations.

Brillouin zone in Fig. 3(a). The value could be smaller if we use a finer momentum grid. On each surface, there exists a pair of Fermi arcs connecting to the bulk states of TPFs at $(k_y = 0, k_z = \pm\pi/2)$. The number of Fermi arcs is consistent with the fact that TPFs are monopoles of the Berry curvature with charge ± 2.

To investigate the robustness of the Fermi arcs, we employ the stacked-layer construction [25] in which the disorder potential is applied only in the x direction (see Appendix B). This allows us to study the evolution of the Fermi arcs with disorder and, in turn, to compute the local density near the momentum $k' = (k_y = -\pi/2, k_z = 0)$, which is one of the furthest momenta away from the TPFs. We choose this k point because the surface Fermi arcs at this point can have the least overlap with the bulk contributions of TPFs. The dispersion for the slab near k' is shown in Fig. 4. It is plotted along the diagonal that runs from $k' - (\delta k, \delta k)$ to $k' + (\delta k, \delta k)$, where $\delta k = \pi/5$. The flat band shows a finite bandwidth. Thus, in this range of momentum, the Fermi arcs can only be isolated
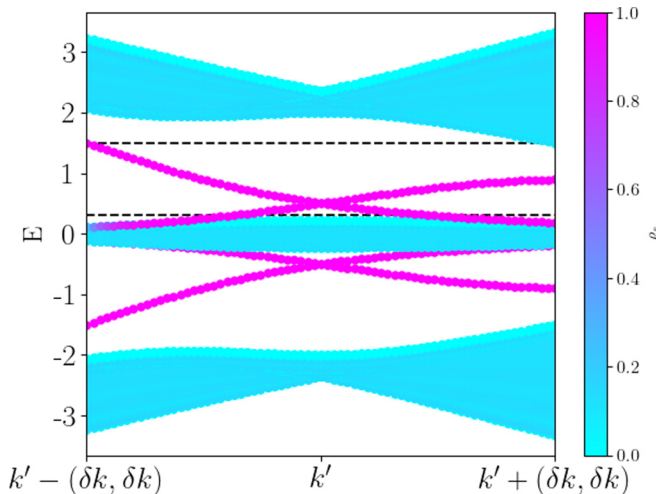

FIG. 4. Energy spectrum of the slab. The horizontal black dashed lines denote $E = 0.3$ and $E = 1.5$. There are 100 lattice site along the x direction. The color on the curve represents surface density. $k' = (k_y = -\pi/2, k_z = 0)$ and $\delta k = 10\frac{2\pi}{N}$, $N = 100$.

from bulk for $0.3 < E < 1.5$. The highest-energy states of the Fermi arcs (megenta curves) eventually merge with bulk states (cyan curves) when momentum is away from k'.

When the disorder strength increases, the Fermi arcs at k' gradually penetrate into bulk. We calculate the ratio of the bulk (ρ_b) and surface (ρ_s) density to quantify this disorder-induced penetration as a function of energy and disorder strength. The definition of $\rho_{b/s}$ is

$$\rho_{b/s} = \sum_{k_y, k_z} \sum_i \rho_{b/s}^i(k_y, k_z), \tag{7}$$

where the first sum is performed over the neighboring k points near k', within the range of $[k_y' - \delta k, k_y' + \delta k]$ and $[k_z' - \delta k, k_z' + \delta k]$. Here we choose $\delta k = 10\frac{2\pi}{N}$, where $N = 100$ is the number of k-points along each direction. Furthermore, i denotes the states within the energy range of $E \leqslant E_i < E + \Delta E$, where ΔE was set to be 0.1 as for the Fermi arcs shown in Fig. 3(a). $\rho_{b/s}^i(k_y, k_z)$ is defined as

$$\rho_b^i(k_y, k_z) = \sum_{x=d}^{L-d} \sum_{o=1}^3 |\langle \psi_i(k_y, k_z)|x, o\rangle|^2, \tag{8}$$

$$\rho_s^i(k_y, k_z) = 1 - \rho_b^i(k_y, k_z), \tag{9}$$

where $L = 100$ is the thickness of the slab and $d = L/20$ is the number of layers that are considered as top/bottom surfaces. The diagram showing this ratio is given in Fig. 3(b). In the clean limit, i.e., $W = 0$, the bulk density vanishes for $0.3 < E < 1.5$, the energy range where the Fermi arcs are isolated from the bulk states. Outside this range, the bulk states coexist with Fermi arcs near k'. As W becomes larger, the Fermi arcs gradually penetrate into bulk, and ρ_b increases. The Fermi arcs can carry a large surface Berry curvature $\Omega_x(\vec{k})$ [23]. As is well known, in the presence of an external electric-field $\vec{E}$, the Berry curvature in momentum space adds the so-called anomalous velocity term in the equations of motion that describe the propagation of Bloch wave-packets $-\frac{e}{\hbar}\vec{E} \times \vec{\Omega}(\vec{k})$ [33–35]. Since the anomalous velocity is perpendicular to the electric field, it can lead to a variety of Hall-like effects. We calculate the surface BC for the Fermi arcs on the top surface of the slab and investigate the effect of disorder. The Fermi arcs are the states with the largest weight on the surface, denoted by ψ_a. Figure 5 shows the Fermi arcs and the surface BC at $E = 0.3$ for $W = 0, 1, 2, 4$. In the clean limit, we find that BC of each arc is odd in k_z, $\Omega_x(k_y, k_z) = -\Omega_x(k_y, -k_z)$. Such a bipolar configuration of BC is due to the mirror symmetry in the z-direction, i.e., $H(-k_z) = H(k_z)$, according to Eqs. (1) and (2). The BCs on the top (t) and bottom (b) surfaces are related by the inversion symmetry of the slab $\Omega_{x,t}(k_y, k_z) = \Omega_{x,b}(-k_y, -k_z)$. Since the BC is proportional to the matrix element of $\frac{\partial H}{\partial k_z}$, the Berry curvature is odd in k_z. Therefore, the surface Hall conductivity, which is proportional to the sum of the Berry curvature in the surface BZ, is exactly zero.

Figure 5(b) shows that, for relatively weak disorder ($W = 1$), the Fermi arcs retain their sharpness. However, negative (positive) surface Berry curvature arises near the surface projection of the positively charged (negatively charged) bulk node. The mixture of positive and negative surface Berry curvatures is more obvious as disorder strength increases as
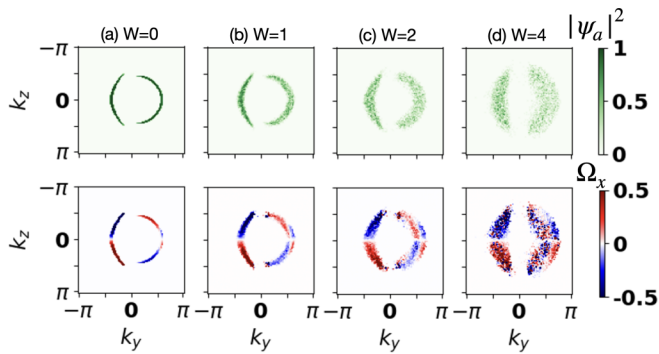
FIG. 5. Fermi arcs (top panel) and the Berry curvature carried by the Fermi arcs (lower panel) on the top surface for disorder (a) $W = 0$, (b) $W = 1$, (c) $W = 2$, and (d) $W = 4$. For (b)–(d), we have avraged over 20 disorder realizations. At stronger disorder the distribution of Fermi arcs is rather sparse. According to Fig. 3(b), the Fermi arcs have penetrated into bulk at $W = 4$.

shown in Figs. 5(c) and 5(d). We note that the k_z-reflection symmetry is broken, and, thus, the Berry curvature is no longer an odd function in k_z when the potential disorder has distribution in the k_y and k_z directions in the momentum space.

Finally, we remark that even when the Hall conductivity vanishes in experiments, the intrinsic geometry of the quantum electron wave functions can still be probed via the nonlinear Hall effect, a direct measure of the Berry curvature dipole. In our case the surface BC dipole defined as

$$D_i = - \int d^2\vec{k} \, \Omega_x(\vec{k})[\partial_{k_i} f_0(\vec{k})], \tag{10}$$

where $f_0(\vec{k})$ is the Fermi-Dirac distribution. The above equation describes the first-order moment of the Berry curvature over occupied states near the Fermi energy. When the boundary is open along the x direction, the mirror symmetry in the z direction forces the surface BC dipole to be $D_y = 0$ and $D_z \neq 0$ (see Appendix C). This results in a transverse charge current along the y direction in second-order response to an external electric field along the z direction. By using the stacked-layer construction, we also numerically find the surface BC dipole could be enhanced with disorder. The interplay between the disorder and the quantum geometric aspects of the Fermi-arcs' electronic structure is experimentally relevant in all BC-driven phenomena, such as the nonlinear anomalous Nernst effect [36] and the surface contributions to the orbital magnetic moment [37]. These are certainly interesting subjects for future investigation.

V. CONCLUSION

We have studied the DOS and Fermi arcs of a disordered three-band tight-binding model that hosts TPFs. Using the lattice model, rather than the low-energy model, we are able to investigate the effect of internode scattering. We found that the inter-TPF scattering is the main mechanism for destroying the

single TPF physics. Nonetheless, there exists a finite-energy window in which the Fermi arcs and the surface Berry curvature remain sharp in the weak disorder limit. These results suggest that the TPFs in the family of transition-metal silicides are robust against disorder. Furthermore, we show that even when the Hall conductivity carried by the Fermi arc states is zero due to mirror symmetry, a finite surface Berry curvature dipole can still exist, leading to the nonlinear Hall effect. The disorder effects on the nonlinear responses, such as the nonlinear anomalous Nernst effect and photocurrent would be interesting directions for future research.

Lastly, we would like to note that the realization of TPFs has also been proposed in optical lattices [38]. In ultracold atomic systems, disorder can be implemented by using laser speckle patterns [39]. In addition, the spectrum can be probed using the methods of time-of-flight imaging and Bragg spectroscopy [39], and the surface Berry curvature can be mapped by extending the techniques applied for two-dimensional lattices [40]. Thus, the disorder effects on TPFs discussed in the paper could be investigated using ultracold atoms in optical lattices.

APPENDIX A: BERRY CURVATURE TRANSFER

The accumulated Chern number for the lowest-energy band (C^{3D}), contributed from each k_z layer, is given by [41]

$$C^{3D} = \frac{1}{\pi} \int_{k_1}^{k_2} dk_z C(k_z), \tag{A1}$$

where $k_{1,2}$ are the two TPF nodes. C^{3D} as a function of λ is shown in Fig. 6.

APPENDIX B: STACKED-LAYER CONSTRUCTION

Here we review the recently introduced stacked-layer construction [25] which is used to study the robustness of the Fermi arcs against disorder. We consider a slab geometry, infinite along the y and z directions and impose an open boundary in the x direction. This allows us to study the Fermi arc states on the (k_y, k_z) plane. In the clean limit, the lattice Hamiltonian reads

$$H^{\text{lat}}(k_y, k_z) = \sum_x [h(k_y, k_z)|x\rangle\langle x| + U(k_y, k_z)|x+1\rangle\langle x| + U^\dagger(k_y, k_z)|x\rangle\langle x+1|], \tag{B1}$$

where

$$h(k_y, k_z) = \begin{pmatrix} 2 - \cos(k_y) - 2\cos(k_z) & -2\cos(k_y) & i\lambda e^{-i(\phi+\pi/4)}\sin(k_y) \\ -2\cos(k_y) & -2 + \cos(k_y) - 2\cos(k_z) & -i\lambda e^{-i(\phi-\pi/4)}\sin(k_y) \\ -i\lambda e^{i(\phi+\pi/4)}\sin(k_y) & i\lambda e^{i(\phi-\pi/4)}\sin(k_y) & 0 \end{pmatrix},$$ (B2)

$$U(k_y, k_z) = \begin{pmatrix} -1/2 & 1 - \sin(k_y) & i\lambda e^{-i(\phi+\pi/4)}/2 \\ 1 + \sin(k_y) & 1/2 & i\lambda e^{-i(\phi-\pi/4)}/2 \\ -i\lambda e^{i(\phi+\pi/4)}/2 & -i\lambda e^{i(\phi-\pi/4)}/2 & 0 \end{pmatrix}.$$ (B3)

$H^{\text{lat}}(k_y, k_z)$ is a $3L \times 3L$ matrix whereas L represents the system size in the x direction. Therefore, we can directly calculate the eigenspectrum and corresponding wave function using exact diagonalization techniques for the lattice Hamiltonian.

To investigate the effect of potential disorder, we add the following Hamiltonian to Eq. (B1):

$$H_{\text{dis}}^{\text{lat}}(k_y, k_z) = \sum_x V(x, k_y, k_z) I_{3\times3} |x\rangle\langle x|.$$ (B4)

Here the disorder potential $V(x, k_y, k_z)$ is drawn independently for each lattice site in the x direction from the uniform distribution $[-W/2, W/2]$. Note that $V(x, k_y, k_z)$ can be also chosen uniformly or independently in the k_y and k_z directions in the momentum space [25].

To extract the Fermi arc states of top and bottom surfaces, we select the state with the largest weight by

$$\arg\max_i \sum_{o=1}^3 \sum_x |\langle\psi_i(k_y, k_z)|x, o\rangle|^2,$$ (B5)

where ψ_i is the ith eigenvector at k_y, k_z, o labels the pseudospin degree of freedom, $x = [L - d, L]$ for the bottom surface and $x = [1, d]$ for the top surface, where $d = 3$.
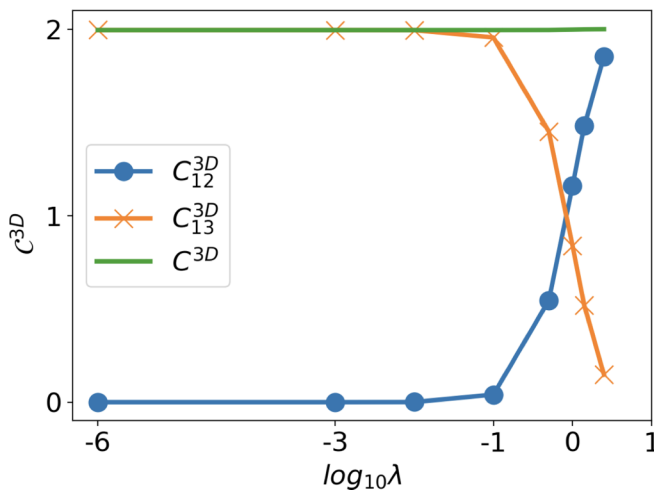

FIG. 6. The accumulated Chern number for the lowest-energy band given by Eq. (A1). The Berry curvature transfers from the element between bands 1 and 3 to bands 1 and 2 as the coupling strength increases.

APPENDIX C: SURFACE BERRY CURVATURE AND SURFACE BERRY CURVATURE DIPOLE

The Fermi arcs of TPFs carry surface Berry curvature $\Omega_x(\vec{k})$. We have shown the surface BC for the Fermi arcs on the top surface of the slab in Fig. 5 for $E = 0.3$ at $W = 0, 1, 2, 4$. The Fermi arcs and BC for the bottom surface is also shown in Fig. 7.

In our case the Fermi arcs also have a nontrivial surface BC dipole, which can lead to the nonlinear Hall currents in the second-order response to an external electric field. In the presence of a driving in-plane electric-field $E_k = \text{Re}\{\mathcal{E}_k e^{i\omega t}\}$, the DC and second-harmonic generated currents in the second-order nonlinear effect are described as $j_i^{(0)} = \sigma_{ijk}\mathcal{E}_j^*\mathcal{E}_k$ and $j_i^{(2\omega)} = \sigma_{ijk}\mathcal{E}_j\mathcal{E}_k$, respectively. The tensor indices i, j, k span the two-dimensional (2D) coordinates y, z of a slab geometry because we impose open boundary conditions along the x direction of the TPF Hamiltonian. Following previous theoretical works [42,43], we know that when the frequency of the driving electric field is much smaller than the resonant frequency for optical transitions, the nonlinear Hall-like current density corresponding to σ_{ijj} with $i \neq j$ is

$$\vec{j}^{(0)} = \frac{e^3\tau}{2\hbar^2(1 + i\omega\tau)}\hat{x} \times \vec{\mathcal{E}}^*(\vec{D} \cdot \vec{\mathcal{E}}),$$ (C1)

$$\vec{j}^{(2\omega)} = \frac{e^3\tau}{2\hbar^2(1 + i\omega\tau)}\hat{x} \times \vec{\mathcal{E}}(\vec{D} \cdot \vec{\mathcal{E}}),$$ (C2)

where $\vec{D}$ is the 2D surface BC dipole and τ is the relaxation time.

We now discuss how the symmetries affect the BC dipole of the surface states considered in this paper. In two dimensions, the BC dipole is a pseudovector, and it has been shown
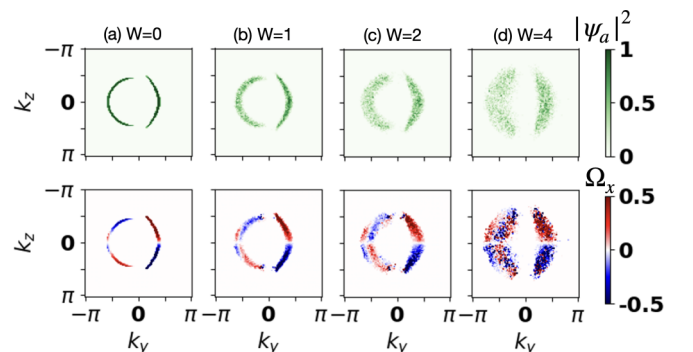

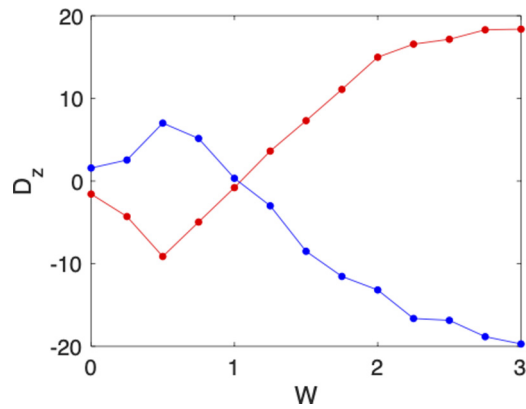FIG. 7. The same plots as in Fig. 5 for the bottom surface of the slab.

FIG. 8. The surface Berry curvature dipole D_z on the top/bottom surface as a function of disorder strength W. Here we consider the Fermi energy at $E = 0.3$, the thickness $L = 20$, and average D_z over 400 disorder realizations.

that the highest symmetry of a 2D crystal that allows for a finite D_i is a single mirror line [43]. When the boundary is open along the x-direction of the model Hamiltonian, the slab has only one mirror symmetry in the z direction, i.e.,

$H(-k_z) = H(k_z)$. Since this mirror symmetry enforces that $\Omega_x(k_y, k_z) = -\Omega_x(k_y, -k_z)$ in the surface Brillouin zone, it is evident that $D_y = 0$ whereas $D_z \neq 0$. By using the stacked-layer construction, we numerically compute the surface BC dipole, setting the Fermi energy to $E = 0.3$ and the thickness $L = 20$ as shown in Fig. 8. Our result shows the the surface BC dipole has a nonmonotonic dependence on disorder.

The surface BC dipole can be understood as follows. Equation (10) can be rewritten as $D_i = \int d^2\vec{k}\delta(E - E_f)\frac{\partial E}{\partial k_i}\Omega_x(\vec{k})$ [44], where $\frac{\partial E}{\partial k_i}$ is the group velocity along the i direction, and $\Omega_x(\vec{k})$ is the BC. Turning on the disorder potential not only effectively varies the chemical potential and bands, but also induces hybridization between the surface states with the bulk states, which changes the localization of the wave function along the direction orthogonal to the surface and, thus, changes the value of the Berry curvature. At the Fermi energy $E = 0.3$, the band dispersion of the surface state does not show a drastic change as a function of disorder. Thus, the major sign change in the BC dipole comes from Berry curvature but not the group velocity. In Fig. 5, it is evident that as disorder increases, the BC with opposite sign against that of the clean limit ($W = 0$) grows substantially from two nodes. Thus, the BC dipole can change sign for a certain value of W.

[1] X.-L. Qi and S.-C. Zhang, Topological insulators and superconductors, Rev. Mod. Phys. **83**, 1057 (2011).

[2] A. H. Castro Neto, F. Guinea, N. M. R. Peres, K. S. Novoselov, and A. K. Geim, The electronic properties of graphene, Rev. Mod. Phys. **81**, 109 (2009).

[3] N. P. Armitage, E. J. Mele, and A. Vishwanath, Weyl and Dirac semimetals in three-dimensional solids, Rev. Mod. Phys. **90**, 015001 (2018).

[4] B. Bradlyn, J. Cano, Z. Wang, M. G. Vergniory, C. Felser, R. J. Cava, and B. A. Bernevig, Beyond Dirac and Weyl fermions: Unconventional quasiparticles in conventional crystals, Science **353**, aaf5037 (2016).

[5] M. Z. Hasan, G. Chang, I. Belopolski, G. Bian, S.-Y. Xu, and J.-X. Yin, Weyl, Dirac and high-fold chiral fermions in topological quantum matter, Nat. Rev. Mater. **6**, 784 (2021).

[6] H. Nielsen and M. Ninomiya, Absence of neutrinos on a lattice, Nucl. Phys. B **185**, 20 (1981).

[7] H. Nielsen and M. Ninomiya, Absence of neutrinos on a lattice, Nucl. Phys. B **193**, 173 (1981).

[8] K. Kobayashi, T. Ohtsuki, K.-I. Imura, and I. F. Herbut, Density of States Scaling at the Semimetal to Metal Transition in Three Dimensional Topological Insulators, Phys. Rev. Lett. **112**, 016402 (2014).

[9] B. Sbierski, G. Pohl, E. J. Bergholtz, and P. W. Brouwer, Quantum Transport of Disordered Weyl Semimetals at the Nodal Point, Phys. Rev. Lett. **113**, 026602 (2014).

[10] C.-Z. Chen, J. Song, H. Jiang, Q.-f. Sun, Z. Wang, and X. C. Xie, Disorder and Metal-Insulator Transitions in Weyl Semimetals, Phys. Rev. Lett. **115**, 246603 (2015).

[11] P. Goswami and A. H. Nevidomskyy, Topological Weyl superconductor to diffusive thermal Hall metal crossover in the b phase of UPt$_3$, Phys. Rev. B **92**, 214504 (2015).

[12] S. Bera, J. D. Sau, and B. Roy, Dirty weyl semimetals: Stability, phase transition, and quantum criticality, Phys. Rev. B **93**, 201302(R) (2016).

[13] J. H. Pixley, D. A. Huse, and S. Das Sarma, Uncovering the hidden quantum critical point in disordered massless Dirac and Weyl semimetals, Phys. Rev. B **94**, 121107(R) (2016).

[14] B. Sbierski, M. Trescher, E. J. Bergholtz, and P. W. Brouwer, Disordered double Weyl node: Comparison of transport and density of states calculations, Phys. Rev. B **95**, 115104 (2017).

[15] J. Klier, I. V. Gornyi, and A. D. Mirlin, From weak to strong disorder in Weyl semimetals: Self-consistent Born approximation, Phys. Rev. B **100**, 125160 (2019).

[16] J. H. Wilson, D. A. Huse, S. Das Sarma, and J. H. Pixley, Avoided quantum criticality in exact numerical simulations of a single disordered Weyl cone, Phys. Rev. B **102**, 100201(R) (2020).

[17] J. Pixley and J. H. Wilson, Rare regions and avoided quantum criticality in disordered Weyl semimetals and superconductors, Ann. Phys. (NY) **435**, 168455 (2021).

[18] J. P. S. Pires, B. Amorim, A. Ferreira, İ. Adagideli, E. R. Mucciolo, and J. M. V. P. Lopes, Breakdown of universality in three-dimensional Dirac semimetals with random impurities, Phys. Rev. Res. **3**, 013183 (2021).

[19] J. P. S. Pires, S. M. João, A. Ferreira, B. Amorim, and J. M. V. P. Lopes, Nodal vacancy bound states and resonances in $\mathcal{T}$-symmetric weyl semimetals: spectral and bulk transport properties, Phys. Rev. B **106**, 184201 (2022).

[20] R. Nandkishore, D. A. Huse, and S. L. Sondhi, Rare region effects dominate weakly disordered three-dimensional Dirac points, Phys. Rev. B **89**, 245110 (2014).

[21] J. Hu, S.-Y. Xu, N. Ni, and Z. Mao, Transport of topological semimetals, Annu. Rev. Mater. Res. **49**, 207 (2019).

[22] Y. Chen, D. L. Bergman, and A. A. Burkov, Weyl fermions and the anomalous Hall effect in metallic ferromagnets, Phys. Rev. B **88**, 125110 (2013).

[23] D. Wawrzik, J.-S. You, J. I. Facio, J. van den Brink, and I. Sodemann, Infinite Berry Curvature of Weyl Fermi Arcs, Phys. Rev. Lett. **127**, 056601 (2021).

[24] Y. Takane, Disorder effect on chiral edge modes and anomalous Hall conductance in Weyl semimetals, J. Phys. Soc. Jpn. **85**, 124711 (2016).

[25] R.-J. Slager, V. Juričić, and B. Roy, Dissolution of topological Fermi arcs in a dirty Weyl semimetal, Phys. Rev. B **96**, 201401(R) (2017).

[26] J. H. Wilson, J. H. Pixley, D. A. Huse, G. Refael, and S. Das Sarma, Do the surface Fermi arcs in Weyl semimetals survive disorder?, Phys. Rev. B **97**, 235108 (2018).

[27] I. C. Fulga and A. Stern, Triple point fermions in a minimal symmorphic model, Phys. Rev. B **95**, 241116(R) (2017).

[28] S. Nandy, S. Manna, D. Călugăru, and B. Roy, Generalized triple-component fermions: Lattice model, Fermi arcs, and anomalous transport, Phys. Rev. B **100**, 235201 (2019).

[29] O. Pal, B. Dey, and T. K. Ghosh, Berry curvature induced anisotropic magnetotransport in a quadratic triple-component fermionic system, J. Phys.: Condens. Matter **34**, 155702 (2022).

[30] A. Weiße, G. Wellein, A. Alvermann, and H. Fehske, The kernel polynomial method, Rev. Mod. Phys. **78**, 275 (2006).

[31] D. Moldovan, M. Anđelković, and F. Peeters, pybinding v0.9.5: a Python package for tight-binding calculations (v0.9.5). Zenodo (2020), https://doi.org/10.5281/zenodo.4010216.

[32] P. Tang, Q. Zhou, and S.-C. Zhang, Multiple Types of Topological Fermions in Transition Metal Silicides, Phys. Rev. Lett. **119**, 206402 (2017).

[33] D. Xiao, M.-C. Chang, and Q. Niu, Berry phase effects on electronic properties, Rev. Mod. Phys. **82**, 1959 (2010).

[34] J. N. Fuchs, F. Piéchon, M. O. Goerbig, and G. Montambaux, Topological Berry phase and semiclassical quantization of cyclotron orbits for two dimensional electrons in coupled band models, Eur. Phys. J. B **77**, 351 (2010).

[35] X. Xu, W. Yao, D. Xiao, and T. F. Heinz, Spin and pseudospins in layered transition metal dichalcogenides, Nat. Phys. **10**, 343 (2014).

[36] X.-Q. Yu, Z.-G. Zhu, J.-S. You, T. Low, and G. Su, Topological nonlinear anomalous Nernst effect in strained transition metal dichalcogenides, Phys. Rev. B **99**, 201410(R) (2019).

[37] G. Sundaram and Q. Niu, Wave-packet dynamics in slowly perturbed crystals: Gradient corrections and Berry-phase effects, Phys. Rev. B **59**, 14915 (1999).

[38] I. C. Fulga, L. Fallani, and M. Burrello, Geometrically protected triple-point crossings in an optical lattice, Phys. Rev. B **97**, 121402(R) (2018).

[39] I. Bloch, J. Dalibard, and W. Zwerger, Many-body physics with ultracold gases, Rev. Mod. Phys. **80**, 885 (2008).

[40] N. Fläschner, B. S. Rem, M. Tarnowski, D. Vogel, D.-S. Lühmann, K. Sengstock, and C. Weitenberg, Experimental reconstruction of the berry curvature in a floquet bloch band, Science **352**, 1091 (2016).

[41] A. A. Burkov and L. Balents, Weyl Semimetal in a Topological Insulator Multilayer, Phys. Rev. Lett. **107**, 127205 (2011).

[42] T. Low, Y. Jiang, and F. Guinea, Topological currents in black phosphorus with broken inversion symmetry, Phys. Rev. B **92**, 235447 (2015).

[43] I. Sodemann and L. Fu, Quantum Nonlinear Hall Effect Induced by Berry Curvature Dipole in Time-Reversal Invariant Materials, Phys. Rev. Lett. **115**, 216806 (2015).

[44] J.-S. You, S. Fang, S.-Y. Xu, E. Kaxiras, and T. Low, Berry curvature dipole current in the transition metal dichalcogenides family, Phys. Rev. B **98**, 121109(R) (2018).